Future Batteries 6 (2025) 100056

Contents lists available at ScienceDirect

Future Batteries

journal homepage: www.sciencedirect.com/journal/future-batteries

Comparative Electrical Characterization of Commercial Sodium-Ion and Lithium-Ion Cells Using Enhanced Ragone Plot Analysis

Pablo Rodríguez-Iturriaga [a,1], Sai Thatipamula [b], Simona Onori [b,*]

[a] Department of Electronics and Computer Technology, University of Granada, Granada, 18071, Andalusia, Spain
[b] Department of Energy Science and Engineering, Stanford University, Stanford, 94305, CA, USA

ARTICLE INFO

Dataset link: http://doi.org/10.17632/j44rvwcpff.1

Keywords:
Sodium-ion battery
Electrical characterization
Lithium-ion
Enhanced Ragone plot
Power-energy analysis

ABSTRACT

Commercial sodium-ion battery (SIB) cells with layered oxide cathodes have recently been introduced to the market. An evaluation of their performance and comparison to existing lithium-ion battery (LIB) technologies at different temperatures and C-rates will provide valuable insights into quantifying their capabilities and identifying potential end-use applications. In this article, we present the electrical characterization of SIB cells with NMF/HC (nickel-manganese-iron/hard carbon) chemistry at different ambient temperatures and C-rates, followed by a critical comparison with existing LIB technologies with the aid of the Enhanced Ragone plot and key metrics, such as discharge capacity, maximum temperature increase, relative discharge time, and discharge efficiency. Thermodynamic characterization results reveal voltage hysteresis in the low state-of-charge region. The electrical and thermal behaviors of galvanostatic discharges across different C-rates and temperatures are also analyzed and linked to the trends in internal resistance. When compared to LIBs, the investigated SIBs show similar power delivery to LFP cells and possess interesting thermal properties: the ability to limit self-heating, and reduce the dependency of electrical behavior on ambient temperature. The tested SIBs may show potential as a promising candidate for operation at temperatures below 10 °C, or in environments with a broad range of operating temperatures without the need for extensive thermal management. Finally, the data supporting the findings of this study are publicly available.

Introduction

The progressive electrification of transportation, coupled with the increasing degree of penetration of renewable energy sources has driven the growing demand for energy storage solutions, catalyzing the development and widespread adoption of lithium-ion battery (LIB) technologies [1]. However, the rapid growth of LIB deployment is projected to result in an increased strain on the supply chain of critical raw materials such as lithium and cobalt due to geographical and geopolitical constraints [2], raising concerns about the availability of sufficient resources to meet the growing demand for energy storage. For this reason, sodium-ion batteries (SIBs), due to their reliance on abundant materials, potential lower costs and reduced safety risks, are emerging as a suitable alternative [3,4]. SIBs are regarded as a drop-in technology, involving analogous production processes and machinery and benefiting from the know-how acquired through LIB development [5–7]. The first commercial SIB cells are now being introduced to the market and may represent a valid energy storage alternative for stationary applications [8] and light-duty vehicles [9], for which energy density plays a less decisive role than the overall cost or safety of the storage system. Their techno-economic competitiveness against LIBs has recently been evaluated in [10] by analyzing cost projections for scenarios considering factors such as technology development, supply chain, and market penetration. Despite cost-competitiveness being highly dependent on fluctuations in the supply chains of critical materials (i.e., lithium, graphite, and nickel) and advancements in SIB energy density, it was shown that, while SIBs may not immediately be price advantageous over LIBs (specifically lithium-iron-phosphate (LFP)) they can play a critical role as a suitable alternative to LIBs in situations of supply chain instability. The goal of this paper is to compare electrical and thermal performance metrics of commonly adopted LIBs against recently commercialized SIB cells with NMF/HC (nickel-manganese-iron/hard carbon) chemistry.

The differences in electrochemical properties between lithium and sodium imply that active materials for LIBs may not be repurposed for SIBs; therefore, the development of tailored electrode materials that are suitable hosts to sodium ions is necessary. It has been shown that

* Corresponding author.
E-mail address: sonori@stanford.edu (S. Onori).
[1] Visiting Scholar at the Department of Energy Science and Engineering, Stanford University.

https://doi.org/10.1016/j.fub.2025.100056
Received 6 November 2024; Received in revised form 28 January 2025; Accepted 10 March 2025
Available online 19 March 2025

sodium ions do not intercalate into graphite to a sufficient degree [11–14]; furthermore, its larger atomic radius in comparison to lithium ions results in slower reaction kinetics and greater volume expansion of electrode materials [15,16]. Amorphous hard carbon (HC) has emerged as the most suitable choice due to its high theoretical capacity (300 mAh/g) [17] and its low voltage plateau (≤0.1 V) vs. Na/Na^+ [18]. Although sodium storage mechanisms in HC are under debate [18,19], intercalation between graphitic layers as well as pore filling have been suggested as storage mechanisms to explain the low-voltage HC plateau [20,21], whereas the sloping profile may be ascribed to the adsorption of sodium ions at defect sites [14]. As for the cathode, three main material categories are usually adopted: Prussian Blue Analogues (PBAs), polyanionic compounds, and transition metal layered oxides [22]. PBAs have low cost, high rate capability, thermal safety and remarkable cycling stability [23,24], and have been incorporated into commercial SIB cells [25], with the disadvantage of a low energy density (23 Wh/kg). PBAs can also be realized in a Na-rich form, known in this case as Prussian White Analogues (PWAs) [15] with higher energy density when employed in conjunction with non-aqueous electrolytes [26,27]. As a result, a SIB cell prototype has been presented by Altris claiming an energy density of 160 Wh/kg [28], which is pending commercialization. Nevertheless, the stable operating window of PWAs is restricted to a small temperature range [29] due to severe side reactions at high temperatures, as well as sluggish kinetics at low temperatures resulting in diminished performance.

Polyanionic compounds are another candidate for SIB cathodes. In particular, sodium-vanadium-fluorophosphate (NVPF) constitutes an interesting option because of a higher working potential vs. Na/Na+ (3.9 V) and higher specific capacity (128 mAh/g) [30], as well as fast ionic diffusion [31], which enables high rate capability. However, the presence of vanadium, which is expensive and toxic, along with a limited cycle life [32] and energy density (68 Wh/kg) [33], are significant drawbacks to their widespread adoption. As a result, considerable attention has been directed towards transition-metal layered oxides as positive electrode materials [34]. These cathodes exhibit a sloping voltage profile within a higher voltage window along with a greater theoretical capacity (≥150 mAh/g) [35,36], resulting in higher energy density compared to PBA and polyanionic compounds. In particular, cells with a nickel-manganese-iron (NMF) cathode have recently been commercialized [37,38].

Commercial cells with an NMF cathode and a HC anode (NMF/HC) have recently been characterized by Laufen et al. [37]. They performed electrochemical characterization tests in order to determine electrode and electrolyte compositions, as well as geometrical properties and active material structure. Additionally, impedance, C-rate, float current and continuous cycling measurements were performed on full cells at 25 °C. Their results indicate that cell impedance increases monotonically with decreasing state-of-charge (SOC), showing a larger impedance variation at low SOCs in comparison to high SOCs. Furthermore, they showed that this commercial cell exhibits remarkable rate capability and a high degree of discharge capacity retention for current rates up to 5C, whereas larger charging currents were shown to trigger cell failure due to current interrupt device activation attributed to gas generation via side reactions. The study concluded that the techniques and models used for analyzing and characterizing LIBs are transferable to SIBs. Furthermore, another commercial cell with the same chemistry by a different manufacturer was studied by Bischof et al. [38], where an analysis of rate performance, temperature increase and cell impedance was performed at 25 °C as a function of the current rate and the total electrode thickness. A brief comparison was made with respect to established LIB chemistries based on the previous metrics. In both cases, the tested cells showed remarkable rate capabilities, although significant self-heating was documented. Finally, we identify two gaps in the literature regarding the characterization of commercial SIB cells with NMF cathode and HC anode:

1. Performance analysis has been conducted at 25 °C alone, but significant self-heating has also been reported for this chemistry [37,38], quantified as the maximum temperature increase as a function of the C-rate [39]. Therefore, characterization results obtained at different controlled temperatures are necessary to properly evaluate cell behavior.
2. A comparison with different LIB chemistries at different temperatures has yet to be carried out, which could provide key insights for assessing potential use cases.

The Ragone plot [40] is a well-established method to compare different storage technologies according to the specific power and specific energy that can be extracted from a device from its fully charged state. However, these properties may depend significantly on temperature and discharge rate. For this reason, the standard Ragone plot is sometimes extended to create an Enhanced Ragone plot [41] to include these characteristics and provide a full picture of the performance of the storage technologies under study. Other authors have suggested extending the Ragone plot by also incorporating information about lifetime (ENPOLITE: energy–power–lifetime–temperature) [42], although aging information is encoded in just one parameter despite the influence of multiple factors.

In this article, we present the electrical characterization of thermodynamic, dynamic and rate properties of a commercial SIB cell at 5 °C, 25 °C and 35 °C, to garner practical insight into the electrical and thermal behavior of this technology. Furthermore, the performance of the tested SIB cells is compared with three different well-established LIB chemistries by means of the Enhanced Ragone plot. Given that the investigated SIBs show qualitatively similar behavior to LFP, a more in-depth comparison between both is conducted via the computation of additional performance metrics in order to inform about potential applications and use-case scenarios. It is noted that, from here on, the term ‘SIB’ is employed to refer to the NMF/HC chemistry and therefore, the results and conclusions presented herein may not be directly applicable to other SIB chemistries.

This paper is organized as follows: the experimental setup and tests are outlined in “Experimental work”. Next, the characterization results are presented and analyzed, and the relevant metrics for the comparison to LIB chemistries are defined and computed in “Results and discussion”. Finally, the main takeaways are summarized and the challenges from a modeling and application perspective are stated. It is emphasized that the data that support the findings of this study are openly available, as outlined in “Conclusion”. All the data presented in this work were specifically collected for this publication and are freely available to users in http://doi.org/10.17632/j44rvwcpff.1.

Experimental work

The experimental campaign was conducted on cylindrical-format SIB cells manufactured by Shenzhen Mushang Electronics (NA18650-1250) with a nominal voltage of 3.0 V and a rated capacity of 1250 mAh (minimum 1200 mAh) at their nominal C/2 discharge rate within the upper voltage (V_{charge}) and lower voltage ($V_{discharge}$) limits of 3.8 V and 1.5 V, respectively. This SIB allows continuous discharge currents up to 8C (10 A) in the temperature range of 10 °C to 50 °C, as well as continuous charge currents up to 5C (6.25 A) in the range of 20 °C to 45 °C (see Table 1). The standard constant-current constant-voltage (CC-CV) charging protocol employs a charging current I_{charge} of C/2 with a C/50 current cutoff for the CV stage at V_{charge}. The cells were experimentally tested on a multichannel Arbin LBT21024 tester at the Stanford Energy Control Laboratory, at Stanford University, CA (USA) [41]. All the experiments were performed under a temperature-controlled environment with the aid of an IncuMax IC-500R environmental chamber by Amerex Instruments. The temperatures inside the environmental chamber and on the cell surface were measured with Type T thermocouple sensors, manufactured by Omega,

Table 1
Specifications of the tested SIB cell.

Chemistry	NMF/HC	
Weight $M_{nom,cell}$ [g]	37	
Nominal voltage V_{nom} [V]	3.0	
Nominal capacity Q_{nom} [Ah]	1.25	
Upper cutoff voltage V_{charge} [V]	3.8	
Standard charge current I_{charge} [A]	0.625	
Lower cutoff voltage $V_{discharge}$ [V]	1.5	
Max. cont. discharge current $I_{discharge}$ [A]	10 (8C)	Sample cell

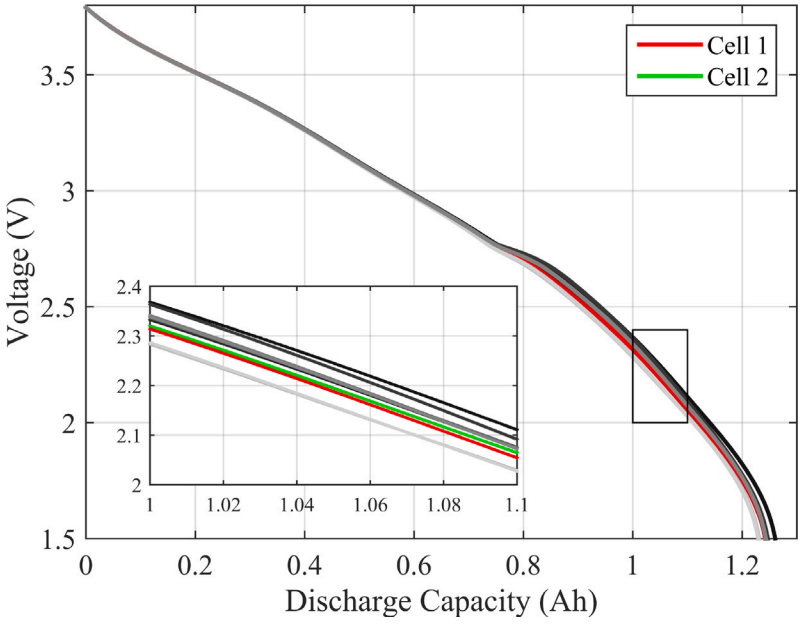

Fig. 1. C/20 discharge profiles of the 10 SIB cells in the batch and their spread. The selected cells (Cell 1 and 2) are plotted in color, while the rest are plotted in grayscale. Inset details voltage fluctuations in the low SOC region (80% ≤ SOC ≤ 88%), ascribed to hard carbon. (For interpretation of the references to color in this figure legend, the reader is referred to the web version of this article.)

and transmitted through the Arbin auxiliary channel to the thermal measurement system. Additional details about the experimental setup may be found in previous work [41].

A batch of n = 10 SIB cells was initially subjected to thermodynamic testing conditions, comprising one full charge and discharge cycle at C/20 (0.0625 A) in order to assess manufacturing-induced cell-to-cell variability, resulting in a capacity of 1243.2 ± 8.2 mAh (±0.66%). Despite acceptable cell-to-cell variation in capacity, significant heterogeneity was observed in the voltage profiles below 40% SOC, ascribed to the sloping voltage region due to hard carbon, as shown in Fig. 1. For this reason, two cells (referred to as Cell 1 and Cell 2 from here on) with similar voltage responses (≤25 mV spread below 40% SOC) were selected for characterization to ensure that the results presented are consistent and representative.

The experimental tests were designed to characterize the electrical and thermal behavior of the investigated SIB cells across temperatures and C-rates of operation, as well as assess their performance in comparison to well-established LIB chemistries in a broad range of operating conditions. The experimental campaign is composed of three sequential tests described below, all of which were carried out at controlled ambient of 5 °C, 25 °C and 35 °C.

1. **Thermodynamic characterization**. This test consists of one charge and discharge cycle at a constant rate of C/50 (25 mA), with the purpose of obtaining the quasi Open Circuit Voltage (q-OCV) vs. SOC relationship, as well as incremental capacity (IC) features [43]. In order to ensure a consistent initialization, cells were charged to 100% SOC by means of the standard CC-CV protocol defined above, followed by a 1-h rest.
2. **Dynamic characterization**. Hybrid Power Pulse Characterization (HPPC) tests were performed to elucidate the dynamic behavior of the investigated cells [39]. The designed protocol consists of 10 discharge pulses at 1C, each followed by a one-h relaxation period and two 10-s charge and discharge pulses at 2C at evenly spaced SOCs, with the goal of measuring the internal resistance at SOCs 10% through 90% in 10% SOC increments.
3. **Galvanostatic characterization**. Galvanostatic discharge tests at increasing C-rates were conducted so as to gauge the energy and power delivery capabilities of the investigated cells. This test is composed of five stages that are repeated for each discharge C-rate in the set: 1C, 2C, 3C, 5C, and 8C.

   (a) 1-h rest for thermal stabilization.
   (b) CC charge at C/2 up to V_{charge}.
   (c) CV hold with a C/50 current cutoff.
   (d) 1-h rest for thermal and voltage stabilization.
   (e) CC discharge at a prescribed C-rate.

A similar characterization campaign was performed previously in [39,41] for cells with three different LIB chemistries: LFP/Gr ANR26650m1-B model by A123 Systems, NMC/Gr INR21700-M50 model by LG Chem and NCA/Gr NCR-18650B model by Panasonic, whose specifications are detailed in Table 2. The results from the design of experiments specified in Table 3 are employed for a comprehensive performance comparison in the following sections. A summary of the experimental setup and tests performed in this work is shown in Fig. 2.

Table 2
Specifications of the SIB cells and LIB cells with three different chemistries employed in this work.

	SIB	LIB	LIB	LIB
Chemistry	NMF/HC	LFP/Gr	NMC/Gr	NCA/Gr
Weight $M_{nom,cell}$ [g]	37	76	68	47.5
Nominal voltage V_{nom} [V]	3.0	3.3	3.63	3.6
Nominal capacity Q_{nom} [Ah]	1.25	2.5	4.85	3.35
Upper cutoff voltage V_{charge} [V]	3.8	3.6	4.2	4.2
Standard charge current I_{charge} [A]	0.625	2.5	1.455	1.625
Lower cutoff voltage $V_{discharge}$ [V]	1.5	2	2.5	2.5
Max. cont. discharge current $I_{discharge}$ [A]	10 (8C)	50 (20C)	7.275 (1.5C)	6.7 (2C)

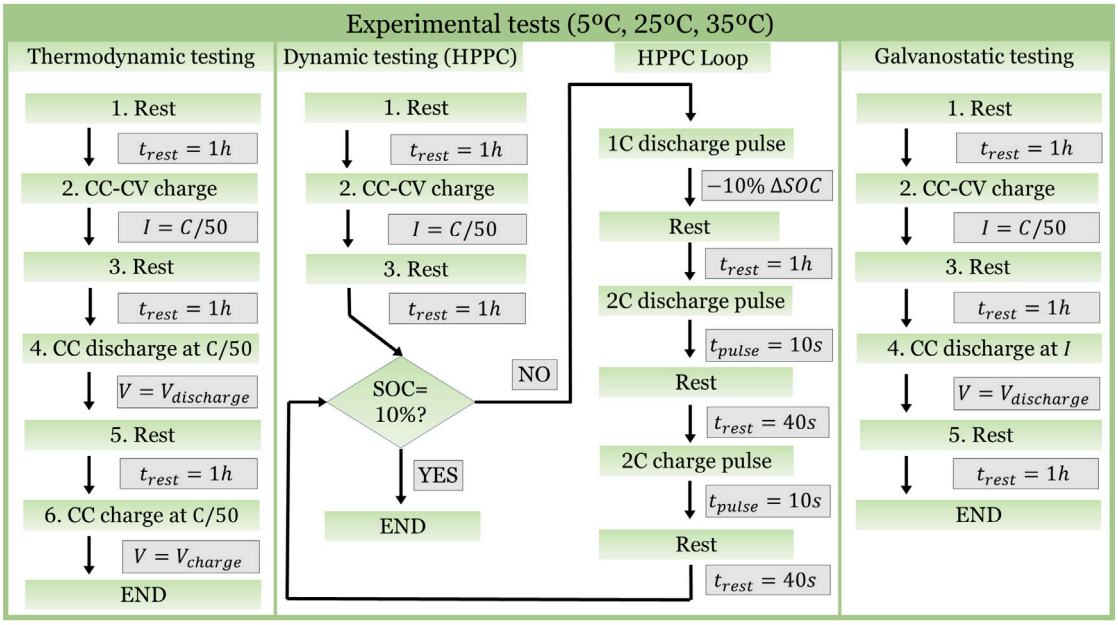

Fig. 2. Summary flowchart of the experimental setup and tests performed in this work. For galvanostatic testing, the procedure is repeated for each C-rate in Table 3.

Table 3
Summary of the design of experiments for temperature and C-rate performance assessment for the SIB and LIB cells compared in this work.

	Applied C-rate								Temperature		
SIB	1C	2C	3C	5C	8C	–	–	–	5 °C	25 °C	35 °C
LFP	1C	2C	3C	5C	–	10C	15C	20C			
NMC	1C	2C	3C	5C	–	–	–	–			
NCA	1C	2C	3C	5C	–	–	–	–			

Results and discussion

Characterization results

In this section, the characterization results corresponding to the experimental schemes described in the previous section are presented and analyzed. Fig. 3 shows (a) q-OCV and (b) incremental capacity profiles obtained from thermodynamic testing at C/50 for Cell 1. As stated in the Experimental section, two cells (Cell 1 and Cell 2) with analogous q-OCV profiles have been selected so as to ensure that the results are representative. However, only the results of Cell 1 are shown in Fig. 3 for the sake of clarity. This cell was electrochemically characterized by Laufen et al. [37] and was determined to be composed of an NMF cathode and a HC anode. The NMF cathode is characterized by two distinct regions: a sloping profile for low degrees of sodiation (cell SOC ≥ 50%, i.e., discharge capacity ≤ 0.625 Ah) and a flatter region at higher degrees of sodiation (cell SOC ≤ 50%, i.e., discharge capacity ≥ 0.625 Ah). Similarly, hard carbon exhibits a sloping region at low degrees of sodiation (cell SOC ≤ 50%) and a plateau for higher degrees of sodiation (cell SOC ≥ 50%). Interestingly, the resulting OCV exhibits a quasilinear profile with SOC, as a consequence of the fact that the sloping region of the cathode approximately matches the flat region in the anode in full-cell configuration and vice versa. This would make SOC estimation from voltage measurements easier when compared to chemistries with much flatter OCV-SOC profiles such as LFP.

A noticeable variation in discharge capacity and voltage level is observed for all three temperatures considered in the low SOC range (i.e., discharge capacity ≥ 1.1 Ah). Given that the voltage profiles in this region follow the sequence of increasing temperatures, and a significantly larger voltage drop is observed at 5 °C as opposed to 25 °C and 35 °C, this behavior is ascribed to large overpotentials due to hard carbon at low SOCs [44]. At a thermodynamic rate such as C/50, the effect of the internal resistance is expected to be negligible, which is corroborated by the overlap of the voltage profile for most of the SOC range. However, at very low SOCs, an increasing internal resistance due to decreasing temperature, causes the cutoff voltage to be reached sooner, which points towards the presence of a substantially large and nonlinear impedance in this SOC window. For this reason, the determination of the entropic coefficient from low-rate galvanostatic data may result in an overestimation at low SOCs given that the measured voltage is not necessarily at equilibrium, which warrants the use of potentiostatic [45] or calorimetric [46] methods.

In addition, an increasing hysteretic voltage gap is observed with decreasing SOC, from approximately 15 mV at 100% SOC to 40 mV at 50% SOC (discharge capacity of 0.625 Ah) up to more than 120 mV at 20% SOC (discharge capacity of 1 Ah). However, at very low SOCs, the voltage gap between the charge and discharge branches may not be fully attributed to thermodynamic hysteresis because a fraction of it is likely due to overpotentials in hard carbon [37]. Unlike some

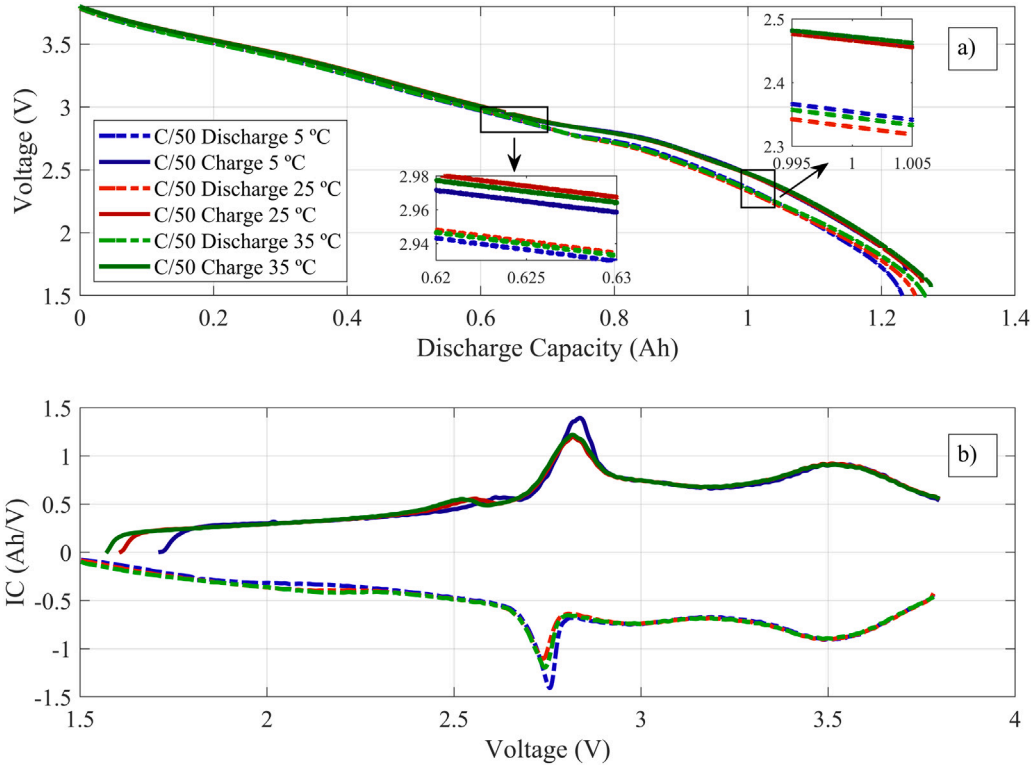

Fig. 3. (a) q-OCV charge and discharge profiles for Cell 1 at 5 °C, 25 °C and 35 °C. Insets depict details of voltage profiles at 50% SOC and 80% SOC (b) Incremental capacity profiles for Cell 1 at 5 °C, 25 °C and 35 °C.

lithium-ion electrode materials such as LFP, where hysteresis can be attributed to phase separation and is present in the flat region [47,48], or graphite, where it is ascribed to consecutive lithium intercalation stages, hysteresis is more prominent in the sloping region of hard carbon rather than in the plateau region in the case of the investigated SIB. Although sodium storage mechanisms in hard carbon are yet not fully understood [18,19], intercalation between graphitic sheets as well as pore filling are possible storage mechanisms to describe the plateau [20,21], whereas the sloping profile may be ascribed to the adsorption of sodium ions at active sites. For this reason, further research is required into the hysteretic behavior in hard carbon.

Incremental capacity (IC) profiles were calculated by first applying a decimation filter to experimental voltage with a window of $\Delta V = 2$ mV, computing the incremental capacity $\Delta Q/\Delta V$ and finally applying a smoothing filter to the result, according to established guidelines [43]. IC results reveal two peaks, which may be associated with phase transformation in the positive electrode due to a flat negative electrode potential in said voltage window. The sloping voltage profile at SOCs $\geq$ 50%, as well as the feature at 3.5 V ascribed to NMF, are reminiscent of a similar behavior in NMC cathodes for LIBs. The gradient in voltage at low SOCs is due to the progressive sodium deintercalation in hard carbon, which results in a constant incremental capacity from 1.8 V to 2.5 V. The large overpotentials mentioned above present in hard carbon at lower temperatures are understood to be the cause of a different IC peak amplitude at 5 °C.

Regarding dynamic characteristics, internal resistance values as a function of SOC, temperature and time interval Δt are shown in Fig. 4, where $\Delta t = 0.1$ s, 1 s, 3 s, 10 s. $R_{int}(SOC, T, \Delta t)$ values are calculated as the average of the pulse resistance calculated from charge and discharge current pulses, according to Eq. (1):

$$R_{int}(SOC,T,\Delta t)\Big|_{charge} = \frac{V(t_0+\Delta t)-V(t_0)}{I(t_0+\Delta t)-I(t_0)}\Bigg|_{charge} \tag{1a}$$

$$R_{int}(SOC,T,\Delta t)\Big|_{discharge} = \frac{V(t_0+\Delta t)-V(t_0)}{I(t_0+\Delta t)-I(t_0)}\Bigg|_{discharge} \tag{1b}$$

$$R_{int}(SOC,T,\Delta t) = \frac{R_{int}(SOC,T,\Delta t)\Big|_{charge} + R_{int}(SOC,T,\Delta t)\Big|_{discharge}}{2} \tag{1c}$$

where t_0 denotes the instant where the current pulse starts. A monotonically decreasing trend of internal resistance is observed with increasing SOC. More specifically, it remains approximately constant in the range from 50% to 90% SOC, while growing in a sustained manner below 50% SOC for all temperatures. This asymmetric behavior is qualitatively different from the usual U-shape that is common in many lithium-ion chemistries [49–51].

An interesting insight regarding electrical behavior may be drawn from the impedance values after increasing time intervals. At 25 °C and 35 °C above 50% SOC, the internal resistance remains constant with respect to SOC and increases slightly as the sampling time interval used for its calculation increases. This is indicative of the fact that the electrical behavior in this region is mainly resistive (i.e., ohmic and charge transfer processes) with a slight contribution of constant diffusive overpotentials. This corresponds to the cathode sloping region and the hard carbon plateau. However, below 50% SOC, an increase in the time interval results in a progressively larger impedance, growing non-linearly with decreasing SOC. For instance, the internal resistance at 90% SOC grows from 41.8 mΩ after 0.1s to 49.3 mΩ after 10 s, which is an 18% increase. Conversely, the internal resistance increases from 74.3 mΩ after 0.1s to 119.4 mΩ after 10 s, which constitutes a 61% increase. Additionally, the SOC limit before the onset of impedance growth increases with larger time intervals. This indicates a considerably slower transient electrical behavior in the hard carbon sloping region, in which much larger charge transfer and diffusion overpotentials are observed. An analogous qualitative behavior is noted at 5 °C, although with approximately twice the magnitude in comparison to 25 °C and 35 °C: from approximately 40 mΩ at 25 °C and 35 °C above 50% SOC, to over 80 mΩ at 5 °C in the same SOC range, which is further exacerbated below 50% SOC. As a result, we anticipate that the modeling of dynamic behavior in the lower half of the full SOC

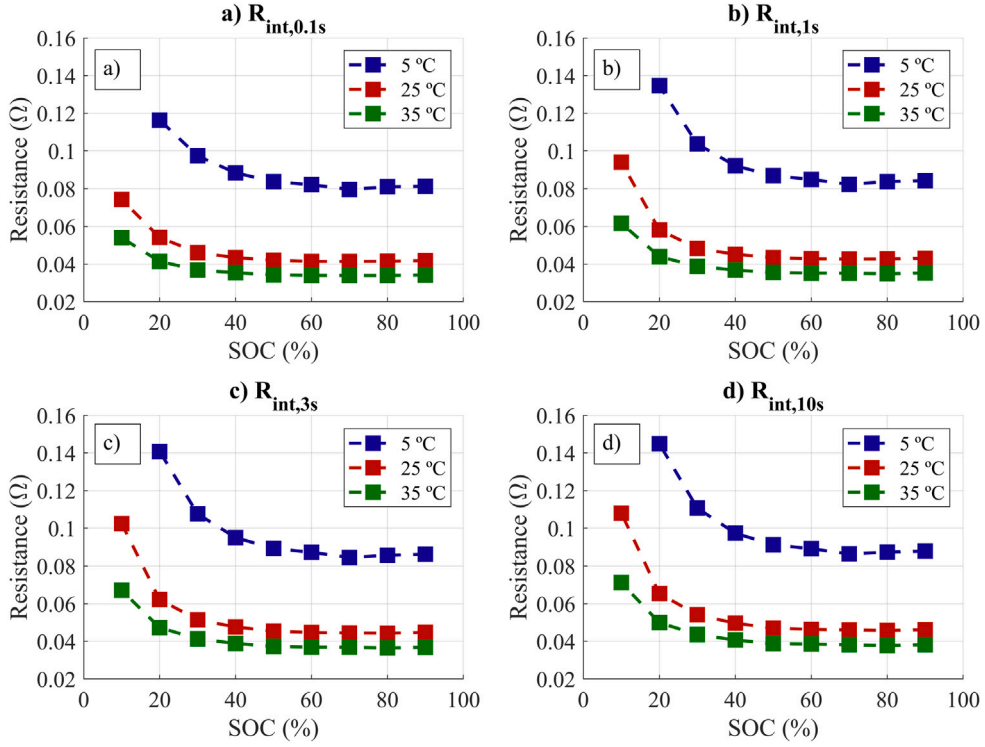

Fig. 4. Internal resistance results as a function of SOC and temperature calculated after (a) 0.1 s, (b) 1 s, (c) 3 s and (d) 10 s, obtained from HPPC testing.

range will pose a greater challenge, exacerbated by the aforementioned hysteretic voltage gap.

Voltage and temperature profiles at 5 °C, 25 °C and 35 °C are shown in Fig. 5 for 1C, 2C, 3C, 5C and 8C discharges, along with the q-OCV profile for reference. Regarding electrical behavior, an interesting feature is especially noticeable at 25 °C and 35 °C, namely the fact that voltage profiles run parallel to each other for SOCs ≥ 40% (discharge capacity ≤ 0.75 Ah) even at C-rates as high as 8C. This is in contrast with the increasingly sloping and smooth voltage profile that is characteristic of some LIB chemistries, such as NMC and NCA [52,53], and may be due to more favorable electrolyte transport properties, as suggested in [37]. Conversely, at SOCs below 20% (discharge capacity ≥ 1 Ah), it is noted that discharge profiles deviate further from the thermodynamic voltage, which is in line with the internal resistance results presented above. Interestingly, this abrupt increase in overpotentials in this SOC range causes the discharge capacity to be less dependent on C-rate. As for thermal behavior, it has to be pointed out that the temperature increase with respect to ambient temperature $\Delta T = T - T_{amb}$ is quantitatively analogous at 25 °C and 35 °C ambient temperatures. This may be partly ascribed to the similar values identified previously for internal resistance, which result in a comparable magnitude of Joule heating. In consequence, it is noted that a 10 °C increase from 25 °C to 35 °C does not result in a significant increase in performance, measured in discharge capacity and temperature increase.

In order to illustrate this behavior more clearly, we calculate the value of the *equivalent impedance*, defined as the deviation from the q-OCV normalized by the current rate of the discharge, and expressed as follows:

$$Z_{eq}(I, T_{amb}, SOC) = \frac{V(C/50, T_{amb}, SOC) - V(I, T_{amb}, SOC)}{I} \quad (2)$$

where the values of the constant discharge current I are set according to Table 3. Lastly, although a qualitatively similar behavior is observed at 5 °C, two key differences are noted. First, the larger internal resistance identified above results in a larger voltage drop and deviation from the corresponding thermodynamic profile. However, the internal resistance identified at this temperature is indeed much larger than that at 25 °C and 35 °C. For this reason, self-heating drastically decreases impedance parameters in this case, neutralizing the large overpotentials caused by low temperatures. As a result, voltage profiles are initially far apart due to the large internal resistance, but progressively coalesce throughout the discharge, yielding almost a constant discharge capacity regardless of the C-rate. A consequence of this decreasing internal resistance effect is that the thermal response is self-controlled to a certain extent: a larger temperature increase is observed at the beginning of the discharges, especially at 5C and 8C, but the temperature increase slows down mid-discharge. As a result, the maximum temperature increase achieved at the end of the discharge is not substantially higher compared to 25 °C and 35 °C.

At 25 °C and 35 °C, it is confirmed that the overpotentials are resistive in nature above SOCs ≥ 40%, whereas a sharp increase is observed at low SOCs. It is noted that the impedance in this region substantially decreases with current rate, which points towards a non-linear overpotential possibly associated with charge transfer. At 5 °C, the effect of self-heating becomes apparent as the equivalent impedance decreases significantly with increasing current rate.

Enhanced Ragone plot

In this section, the performance of the tested SIB cell is compared to well-established LIB chemistries (NMC, NCA and LFP) according to the Enhanced Ragone plot, as well as other relevant metrics. It is reiterated that the term 'SIB' here refers specifically to the NMF/HC chemistry.

The energy E and power P delivered for a specific discharge current I and ambient temperature T_{amb} are computed as follows:

$$E(I, T_{amb}) = \int_0^{t_f} V(I, T_{amb}) I dt \qquad P(I, T_{amb}) = \frac{E(I, T_{amb})}{t_f} \quad (3)$$

where t_f is the final discharge time when the $V_{discharge}$ is reached. Specific values are computed by dividing each metric by the nominal cell weight. It is noted that the results for both cells have been averaged in order to provide a representative value. The Enhanced Ragone plot for NMC, NCA, LFP and the investigated SIB at 5 °C, 25 °C and 35 °C at various discharge rates is shown in Fig. 6.

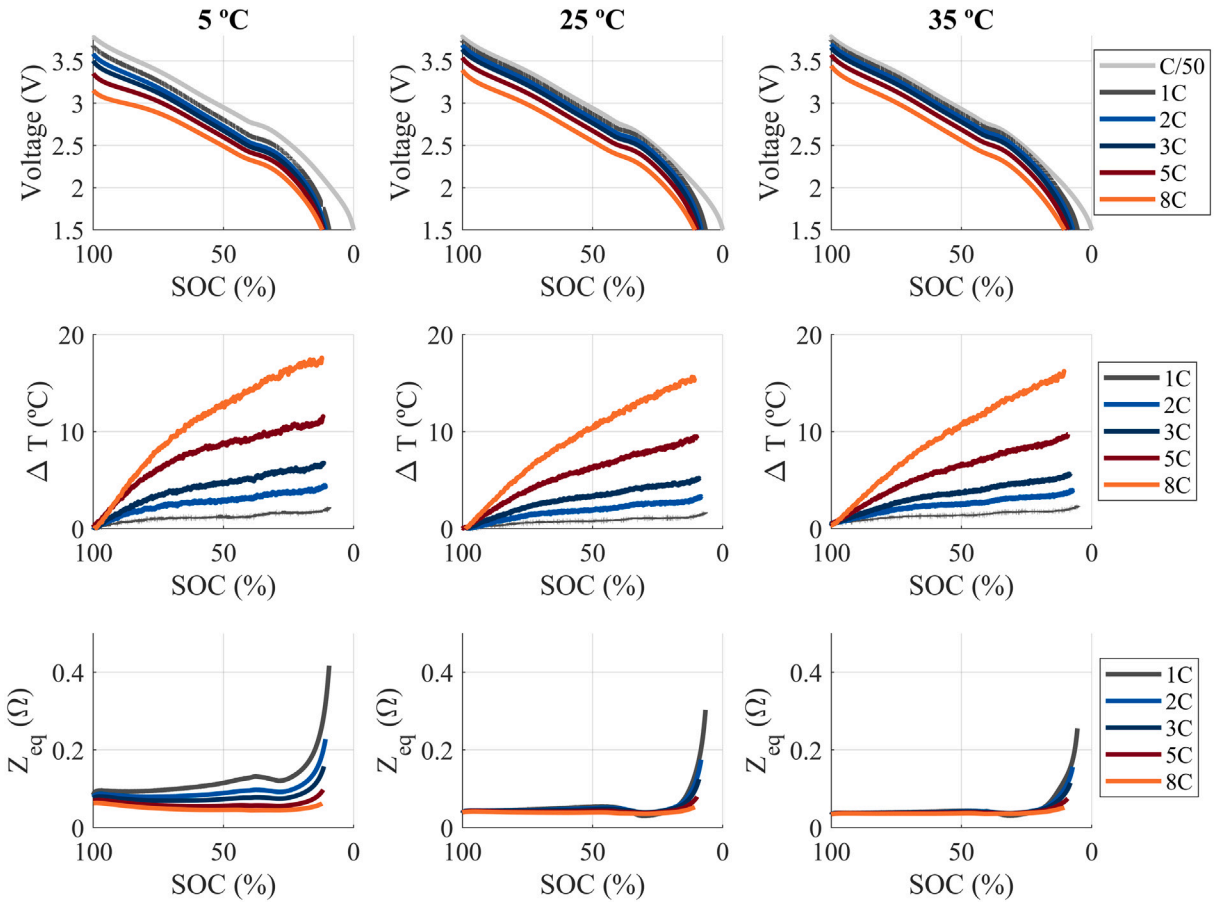

Fig. 5. Cell performance for discharges at 1C, 2C, 3C, 5C and 8C at 5 °C, 25 °C and 35 °C. Voltage, temperature and equivalent impedance profiles averaged over both tested cells are shown.

It is observed that NMC and NCA possess more than double the energy density (over 250 Wh/kg at 25 °C) in relation to LFP and the tested SIB (108 Wh/kg and 97 Wh/kg at 25 °C, respectively) at low C-rates; however, their power capabilities are severely limited due to the fact that high-rate operation is not favored by these chemistries. This is especially prominent in NCA cells, which show a drastic reduction in energy delivered above 3C. Conversely, LFP is able to provide high specific power (over 1 kW/kg) without substantial energy losses, even at rates as high as 20C. For all LIB chemistries, a noticeable drop in performance is noted for 5 °C in comparison to 25 °C and 35 °C. Regarding the investigated SIB, almost identical power capabilities are observed with respect to LFP in the range from 1C to 5C, with a slightly lower specific energy. The maximum power density is just above 700 W/kg, achieved at 8C discharges at 25 °C and 35 °C. Interestingly, the spread in specific energy of the branches corresponding to different temperatures is smaller in the tested SIB in comparison to the considered LIB chemistries.

In light of performance results, it is apparent that the investigated SIB exhibits properties most similar to LFP. In order to provide a more comprehensive comparison and assessment of their capabilities, the following relevant metrics are defined:

- Discharge Capacity (Q_d) at a discharge current I and ambient temperature T_{amb}.

$$Q_d(I, T_{amb}) = \int_0^{t_f} I\,dt \tag{4}$$

- Maximum temperature increase (ΔT_{max}). The constant-current discharge process causes an increase in cell surface temperature due to self-heating. The maximum temperature increase at a discharge current I and ambient temperature T_{amb} is defined as the maximum value of the difference between cell surface temperature T and ambient temperature T_{amb} throughout the discharge. This metric provides valuable insight into cell thermal robustness, defined as the ability of a cell to limit its own self-heating, and therefore entail a reduced risk of thermal runaway.

$$\Delta T_{max} = max(T(I, T_{amb})) - T_{amb} \tag{5}$$

- Relative discharge time (r_d). The relative discharge time at a discharge current I and ambient temperature T_{amb} is the ratio between the experimental duration of the corresponding discharge process and the nominal discharge time $t_{f,nom}$ as a function of the applied C-rate (e.g., 1 h for 1C, 30 min for 2C, etc.). This metric quantifies retention of nominal discharge capacity with increasing C-rate, as the corresponding overpotentials may cause the cell to reach the lower cutoff voltage sooner than ideally.

$$r_d(I, T_{amb}) = \frac{t_f(I, T_{amb})}{t_{f,nom}} \tag{6}$$

- Discharge efficiency (η_e). The discharge efficiency at a discharge current I and ambient temperature T_{amb} is defined according to [41] as the ratio between the energy delivered in said scenario and the maximum possible energy to be delivered at that temperature, measured at a thermodynamic current rate q-OCV. As the discharge rate increases, overpotentials cause the demanded current to be provided at a progressively lower voltage, thus decreasing the overall energy delivered throughout the process.

$$\eta_e(I, T_{amb}) = \frac{E(I, T_{amb})}{E(q - OCV, T_{amb})} \tag{7}$$

Again, all metrics are first computed and then averaged for both cells to provide a representative value. Results are shown in Fig. 7.

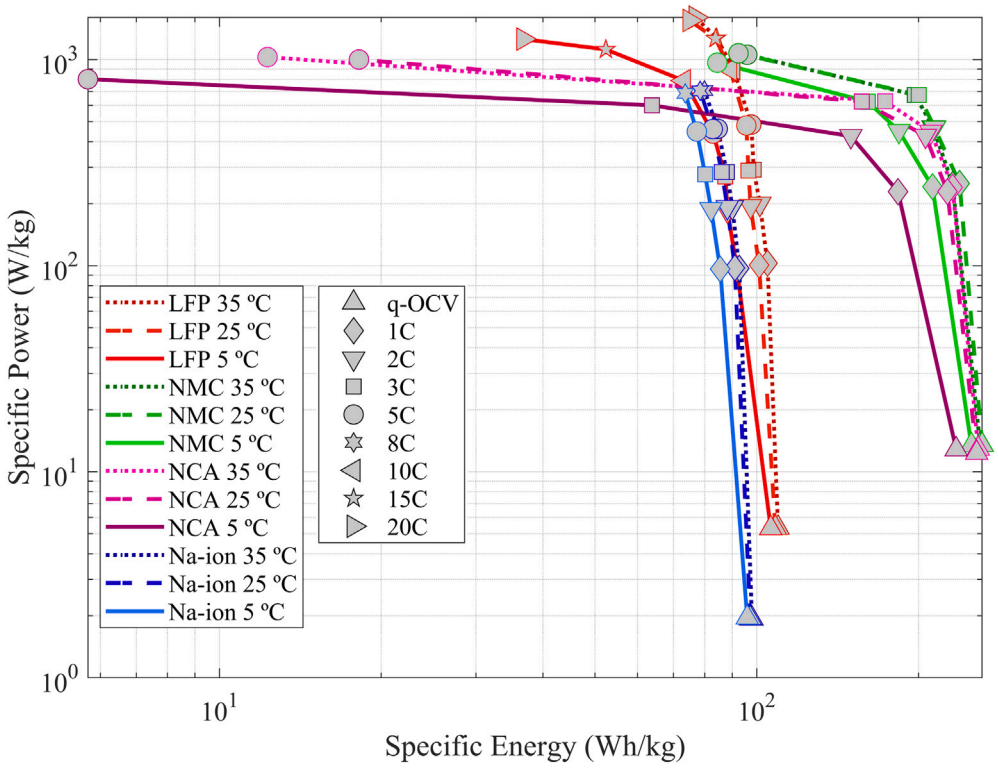

Fig. 6. Enhanced Ragone plot depicting the performance of NMC, NCA, LFP and SIB for the indicated C-rates and temperatures, according to the design of experiment in Table 3. q-OCV indicates the specific power and energy measured in thermodynamic conditions.

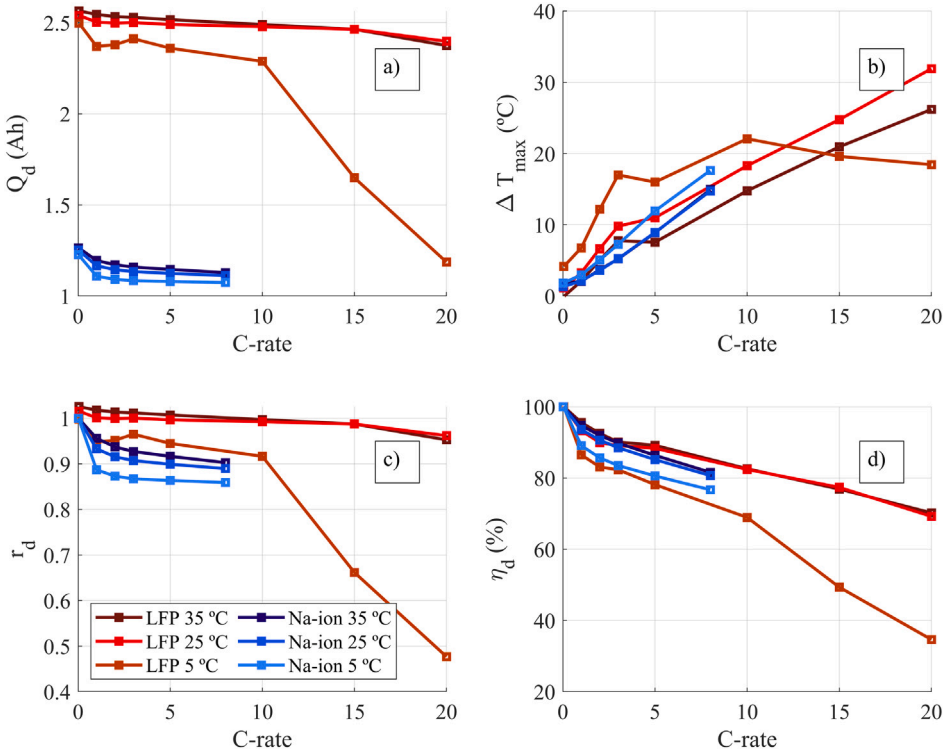

Fig. 7. Comparison between the investigated SIB and LFP with respect to (a) discharge capacity Q_d, (b) maximum temperature increase ΔT_{max}, (c) relative discharge time r_d and (d) discharge efficiency η_d.

Regarding discharge capacity, it is observed that LFP cells are able to deliver a value close to the nominal capacity at 25 °C and 35 °C up to very high C-rates, only showing a slight drop at 20C. In contrast, at 5 °C ambient temperature a drop in performance is noticeable, especially above 10C. As for the tested SIB, a different behavior is observed: discharge capacity drops significantly from C/50 to 1C, but only shows a minor decrease from 1C to 8C, which is attributed to the large overpotentials observed in the low SOC region. A clearer comparison is facilitated by the relative discharge time. In the case of LFP cell, this metric remains close to 1 and only falls to 95% at 20C at 25 °C and 35 °C, whereas at 5 °C it is above 90% up to 10C but drops below 70% and 50% at 15C and 20C, respectively. In the case of the investigated SIB, the relative discharge time shows a slightly more pronounced decrease with C-rate at 25 °C and 35 °C in the region of 90%; however, at 5 °C the effect of self-heating on internal resistance causes the discharge capacity to remain largely constant in the range from 1C to 8C around 86%. Therefore, it is noted that LFP cell performance is more sensitive to lower temperatures than the tested SIB, which shows a more consistent behavior.

The maximum temperature increase reveals interesting trends: while this metric is quasi-linear for the investigated SIB, two regions with different slopes are observed for LFP with the inflection point being at 5C. At said rate, the temperature increases are 7.6 °C, 11 °C and 16 °C for LFP, and 8.9 °C, 8.9 °C and 11.9 °C for the tested SIB, respectively. This leads to postulate that the investigated SIB is more thermally robust than LFP as the temperature responses are less spread out as a function of temperature. As a matter of fact, the tested SIB exhibits less self-heating than LFP at 5 °C ambient temperature.

This behavior is confirmed by the analysis of the discharge efficiency. At 25 °C and 35 °C, both chemistries exhibit similar performance up to 3C, with discharge efficiencies above 89%. It is not until 5C where LFP shows marginally superior performance (88% vs. 85%). However, at 5 °C it has to be pointed out that the investigated SIB outperforms LFP for every shared C-rate. This is a relevant result, as it may reveal low temperature environments, where LIBs are known to struggle, as a potential scenario for the adoption of SIBs. This may also lead to a reduction in hardware and energy consumption associated with thermal management in comparison to LIBs, which may increase their cost competitiveness in specific applications.

Conclusion

Sodium-ion battery technology has emerged as a viable storage technology in recent years, and the first commercial cells are starting to become readily available. For this reason, characterizing and understanding their behavior and performance becomes essential to identify suitable applications. In this article, we first carry out comprehensive characterization tests on a commercial SIB cell (NMF/HC) at different ambient temperatures, and then perform a critical comparison to different LIB chemistries with the aid of the Enhanced Ragone plot and the computation of relevant metrics.

Regarding cell behavior, thermodynamic tests reveal cell-to-cell variability in electrode stoichiometry, which appear to have a larger influence on quasi-OCV profiles than discharge capacity, in addition to voltage hysteresis in the low SOC region. Internal resistance shows an asymmetric dependence on SOC, remaining constant for SOCs above 50% and increasing substantially at low SOCs. Galvanostatic testing at increasing C-rates reveal that cell overpotential is resistive in nature for SOCs above 50%, but highly nonlinear at low SOCs. This causes voltage profiles to run parallel to each other at high to medium SOCs, while a steep voltage drop at low SOCs causes the discharge capacity not to be as dependent on discharge rate. Lastly, the effect of self-heating on electrical performance is considerable at low temperatures; however, this does not lead to a significantly higher temperature increase. For the reasons above, from a modeling and estimation perspective, the main challenges lie in explaining and replicating cell behavior in the low SOC region, along with coupling electrical and thermal performance for operation at low temperatures.

In relation to LIBs, the investigated SIB shows analogous specific power with respect to LFP, with a marginally smaller energy density. Although it exhibits a lower retention of available capacity in relation to nominal capacity, two interesting properties may make it a suitable alternative to LFP for specific applications: thermal robustness and thermal stability. First, the tested SIB cells show a more consistent thermal response in a wide range of ambient temperatures, while LFP displays a larger spread. Similarly, its electrical behavior is not as dependent on ambient temperature as LIBs, which is illustrated by a higher discharge energy efficiency at 5 °C with respect to LFP. As a result, SIB-based storage technologies may constitute a promising candidate for low temperature environments, or applications where a large temperature operating window is expected, while not requiring as complex a thermal management system. Nevertheless, a realistic cycle life assessment remains necessary for a complete evaluation of their performance and selection of applications in comparison to LIBs.

CRediT authorship contribution statement

Pablo Rodríguez-Iturriaga: Writing – original draft, Visualization, Validation, Software, Methodology, Investigation, Formal analysis, Data curation. **Sai Thatipamula:** Writing – review & editing, Validation, Resources, Methodology, Investigation, Formal analysis, Data curation. **Simona Onori:** Writing – review & editing, Validation, Supervision, Resources, Project administration, Methodology, Funding acquisition, Formal analysis, Conceptualization.

Declaration of competing interest

The authors declare that they have no known competing financial interests or personal relationships that could have appeared to influence the work reported in this paper.

Acknowledgments

Pablo Rodríguez-Iturriaga acknowledges grant FPU22/00501 by the Spanish Ministry of Science and Innovation and was a Visiting Researcher at the Department of Energy Science and Engineering at Stanford University. Venkata Saicharan Thatipamula acknowledges support from Chevron through the Chevron Energy Fellowship 2024. Dr. Simona Onori would like to thank the Bits and Watts Initiative within the Precourt Institute for Energy at Stanford University for its partial financial support.

Data availability

The data that support the findings of this study are openly available in Mendeley Data at http://doi.org/10.17632/j44rvwcpff.1.

References

[1] M. Armand, J.-M. Tarascon, Nature 451 (7179) (2008) 652–657, http://dx.doi.org/10.1038/451652a.

[2] E.A. Olivetti, G. Ceder, G.G. Gaustad, X. Fu, Joule 1 (2) (2017) 229–243, http://dx.doi.org/10.1016/j.joule.2017.08.019.

[3] J.-M. Tarascon, Joule 4 (8) (2020) 1616–1620, http://dx.doi.org/10.1016/j.joule.2020.06.003.

[4] K. Chayambuka, G. Mulder, D.L. Danilov, P.H.L. Notten, Adv. Energy Mater. 10 (38) (2020) 2001310, http://dx.doi.org/10.1002/aenm.202001310.

[5] P.K. Nayak, L. Yang, W. Brehm, P. Adelhelm, Angew. Chem. Int. Ed. 57 (1) (2018) 102–120, http://dx.doi.org/10.1002/anie.201703772.

[6] N. Tapia-Ruiz, A.R. Armstrong, H. Alptekin, M.A. Amores, H. Au, J. Barker, R. Boston, W.R. Brant, J.M. Brittain, Y. Chen, M. Chhowalla, Y.-S. Choi, S.I.R. Costa, M.C. Ribadeneyra, S.A. Cussen, E.J. Cussen, W.I.F. David, A.V. Desai, S.A.M. Dickson, E.I. Eweka, J.D. Forero-Saboya, C.P. Grey, J.M. Griffin, P. Gross, X. Hua, J.T.S. Irvine, P. Johansson, M.O. Jones, M. Karlsmo, E. Kendrick, E. Kim, O.V. Kolosov, Z. Li, S.F.L. Mertens, R. Mogensen, L. Monconduit, R.E. Morris, A.J. Naylor, S. Nikman, C.A. O'Keefe, D.M.C. Ould, R.G. Palgrave, P. Poizot, A. Ponrouch, S. Renault, E.M. Reynolds, A. Rudola, R. Sayers, D.O. Scanlon, S. Sen, V.R. Seymour, B. Silván, M.T. Sougrati, L. Stievano, G.S. Stone, C.I. Thomas, M.-M. Titirici, J. Tong, T.J. Wood, D.S. Wright, R. Younesi, J. Phys.: Energy 3 (3) (2021) 031503, http://dx.doi.org/10.1088/2515-7655/ac01ef.

[7] A.N. Singh, M. Islam, A. Meena, M. Faizan, D. Han, C. Bathula, A. Hajibabaei, R. Anand, K.-W. Nam, Adv. Funct. Mater. 33 (46) (2023) 2304617, http://dx.doi.org/10.1002/adfm.202304617.

[8] H. Bai, Z. Song, J. Power Sour. 580 (2023) 233426, http://dx.doi.org/10.1016/j.jpowsour.2023.233426.

[9] A. Rudola, R. Sayers, C.J. Wright, J. Barker, Nature Energy 8 (3) (2023) 215–218, http://dx.doi.org/10.1038/s41560-023-01215-w.

[10] A. Yao, S.M. Benson, W.C. Chueh, Nature Energy (2025) http://dx.doi.org/10.1038/s41560-024-01701-9.

[11] Z. Li, C. Bommier, Z.S. Chong, Z. Jian, T.W. Surta, X. Wang, Z. Xing, J.C. Neuefeind, W.F. Stickle, M. Dolgos, et al., Adv. Energy Mater. 7 (18) (2017) http://dx.doi.org/10.1002/aenm.201602894.

[12] H. Alptekin, H. Au, A.C. Jensen, E. Olsson, M. Goktas, T.F. Headen, P. Adelhelm, Q. Cai, A.J. Drew, M.-M. Titirici, ACS Appl. Energy Mater. 3 (10) (2020) 9918–9927, http://dx.doi.org/10.1021/acsaem.0c01614.

[13] H. Au, H. Alptekin, A.C.S. Jensen, E. Olsson, C.A. O'Keefe, T. Smith, M. Crespo-Ribadeneyra, T.F. Headen, C.P. Grey, Q. Cai, A.J. Drew, M.-M. Titirici, Energy Environ. Sci. 13 (2020) 3469–3479, http://dx.doi.org/10.1039/D0EE01363C.

[14] J.M. Stratford, A.K. Kleppe, D.S. Keeble, P.A. Chater, S.S. Meysami, C.J. Wright, J. Barker, M.-M. Titirici, P.K. Allan, C.P. Grey, J. Am. Chem. Soc. 143 (35) (2021) 14274–14286, http://dx.doi.org/10.1021/jacs.1c06058.

[15] J. Lee, J. Baek, Y. Kim, W. Jeong, H. Kim, G. Oh, Y. Oh, S. Jeong, S. Kansara, B. Sambandam, J.-Y. Hwang, J. Kim, Mater. Today Chem. 33 (2023) 101741, http://dx.doi.org/10.1016/j.mtchem.2023.101741.

[16] Y. Shao, Y. Zhang, N. Jiang, Y. Hao, K. Qu, Y. Zeng, Z. Liu, X. Lu, Y. Li, Q. Yang, J. Qiu, IScience 26 (12) (2023) 108470, http://dx.doi.org/10.1016/j.isci.2023.108470.

[17] X. Chen, Y. Zheng, W. Liu, C. Zhang, S. Li, J. Li, Nanoscale 11 (2019) 22196–22205, http://dx.doi.org/10.1039/C9NR07545C.

[18] Y. Li, A. Vasileiadis, Q. Zhou, Y. Lu, Q. Meng, Y. Li, P. Ombrini, J. Zhao, Z. Chen, Y. Niu, et al., Nature Energy 9 (2) (2024) 134–142, http://dx.doi.org/10.1038/s41560-023-01414-5.

[19] X. Chen, C. Liu, Y. Fang, X. Ai, F. Zhong, H. Yang, Y. Cao, Carbon Energy 4 (6) (2022) 1133–1150, http://dx.doi.org/10.1002/cey2.196.

[20] S. Alvin, D. Yoon, C. Chandra, R.F. Susanti, W. Chang, C. Ryu, J. Kim, J. Power Sour. 430 (2019) 157–168, http://dx.doi.org/10.1016/j.jpowsour.2019.05.013.

[21] X. Zhang, X. Dong, X. Qiu, Y. Cao, C. Wang, Y. Wang, Y. Xia, J. Power Sour. 476 (2020) 228550, http://dx.doi.org/10.1016/j.jpowsour.2020.228550.

[22] M. He, S. Liu, J. Wu, J. Zhu, Prog. Solid State Chem. 74 (2024) 100452, http://dx.doi.org/10.1016/j.progsolidstchem.2024.100452.

[23] C.D. Wessells, R.A. Huggins, Y. Cui, Nature Commun. 2 (1) (2011) http://dx.doi.org/10.1038/ncomms1563.

[24] C. Yan, A. Zhao, F. Zhong, X. Feng, W. Chen, J. Qian, X. Ai, H. Yang, Y. Cao, Electrochim. Acta 332 (2020) 135533, http://dx.doi.org/10.1016/j.electacta.2019.135533.

[25] M. He, R. Davis, D. Chartouni, M. Johnson, M. Abplanalp, P. Troendle, R.-P. Suetterlin, J. Power Sour. 548 (2022) 232036, http://dx.doi.org/10.1016/j.jpowsour.2022.232036.

[26] S. Gourang Patnaik, I. Escher, G.A. Ferrero, P. Adelhelm, Batteries Supercaps 5 (7) (2022) e202200043, http://dx.doi.org/10.1002/batt.202200043.

[27] X. Wu, Z. Jian, Z. Li, X. Ji, Electrochem. Commun. 77 (2017) 54–57, http://dx.doi.org/10.1016/j.elecom.2017.02.012.

[28] Altris-AB, 2023, https://www.altris.se/news/altris-reaches-new-milestone-with-160-wh-kg-battery-cell. (Accessed January 2025).

[29] R. Sun, Y. You, ACS Appl. Mater. Interfaces 15 (38) (2023) 44599–44606, http://dx.doi.org/10.1021/acsami.3c08521, PMID: 37708368.

[30] Y. Subramanian, W. Oh, W. Choi, H. Lee, M. Jeong, R. Thangavel, W.-S. Yoon, Chem. Eng. J. 403 (2021) 126291, http://dx.doi.org/10.1016/j.cej.2020.126291.

[31] M. Wang, X. Huang, H. Wang, T. Zhou, H. Xie, Y. Ren, RSC Adv. 9 (2019) 30628–30636, http://dx.doi.org/10.1039/C9RA05089B.

[32] P. Desai, J. Forero-Saboya, V. Meunier, G. Rousse, M. Deschamps, A.M. Abakumov, J.-M. Tarascon, S. Mariyappan, Energy Storage Mater. 57 (2023) 102–117, http://dx.doi.org/10.1016/j.ensm.2023.02.004.

[33] M. He, A.E. Mejdoubi, D. Chartouni, M. Morcrette, P. Troendle, R. Castiglioni, J. Power Sour. 588 (2023) 233741, http://dx.doi.org/10.1016/j.jpowsour.2023.233741.

[34] Q. Liu, Z. Hu, M. Chen, C. Zou, H. Jin, S. Wang, S.-L. Chou, S.-X. Dou, Small 15 (32) (2019) 1805381, http://dx.doi.org/10.1002/smll.201805381.

[35] B. Xiao, F. Omenya, D. Reed, X. Li, Nanotechnology 32 (42) (2021) 422501, http://dx.doi.org/10.1088/1361-6528/ac12eb.

[36] W. Zuo, A. Innocenti, M. Zarrabeitia, D. Bresser, Y. Yang, S. Passerini, Acc. Chem. Res. 56 (3) (2023) 284–296, http://dx.doi.org/10.1021/acs.accounts.2c00690, PMID: 36696961.

[37] H. Laufen, S. Klick, H. Ditler, K.L. Quade, A. Mikitisin, A. Blömeke, M. Schütte, D. Wasylowski, M. Sonnet, L. Henrich, A. Schwedt, G. Stahl, F. Ringbeck, J. Mayer, D.U. Sauer, Cell Rep. Phys. Sci. 5 (5) (2024) 101945, http://dx.doi.org/10.1016/j.xcrp.2024.101945.

[38] K. Bischof, V. Marangon, M. Kasper, A. Aracil Regalado, M. Wohlfahrt-Mehrens, M. Hölzle, D. Bresser, T. Waldmann, J. Power Sour. Adv. 27 (2024) 100148, http://dx.doi.org/10.1016/j.powera.2024.100148.

[39] E. Catenaro, S. Onori, Data Brief 35 (2021) 106894, http://dx.doi.org/10.1016/j.dib.2021.106894.

[40] D.V. Ragone, SAE Tech. Pap. Ser. (1968) http://dx.doi.org/10.4271/680453.

[41] E. Catenaro, D.M. Rizzo, S. Onori, Appl. Energy 291 (2021) 116473, http://dx.doi.org/10.1016/j.apenergy.2021.116473.

[42] P. Dechent, A. Epp, D. Jöst, Y. Preger, P.M. Attia, W. Li, D.U. Sauer, ACS Energy Lett. 6 (6) (2021) 2351–2355, http://dx.doi.org/10.1021/acsenergylett.1c00743.

[43] M. Dubarry, D. Anseán, Front. Energy Res. 10 (2022) http://dx.doi.org/10.3389/fenrg.2022.1023555.

[44] H. Hijazi, Z. Ye, L. Zhang, J. Deshmukh, M.B. Johnson, J.R. Dahn, M. Metzger, J. Electrochem. Soc. 170 (7) (2023) 070512, http://dx.doi.org/10.1149/1945-7111/ace4fa.

[45] F. Wei, P. Li, Q. Zhang, G. Shao, J. Mao, J. Electrochem. Soc. 169 (5) (2022) 050503, http://dx.doi.org/10.1149/1945-7111/ac6a14.

[46] N. Damay, R. Recoquillé, H. Rabab, J. Kozma, C. Forgez, A. El Mejdoubi, K. El Kadri Benkara, J. Power Sour. 581 (2023) 233460, http://dx.doi.org/10.1016/j.jpowsour.2023.233460.

[47] J. Lim, Y. Li, D.H. Alsem, H. So, S.C. Lee, P. Bai, D.A. Cogswell, X. Liu, N. Jin, Y. sang Yu, N.J. Salmon, D.A. Shapiro, M.Z. Bazant, T. Tyliszczak, W.C. Chueh, Sci. 353 (6299) (2016) 566–571, http://dx.doi.org/10.1126/science.aaf4914.

[48] A. Van der Ven, K.A. See, L. Pilon, Battery Energy 1 (2) (2022) 20210017, http://dx.doi.org/10.1002/bte2.20210017.

[49] C.-H. Doh, Y.-C. Ha, S. wook Eom, Electrochim. Acta 309 (2019) 382–391, http://dx.doi.org/10.1016/j.electacta.2019.04.026.

[50] L. Chen, M. Zhang, Y. Ding, S. Wu, Y. Li, G. Liang, H. Li, H. Pan, Energy Rep. 7 (2021) 3050–3059, http://dx.doi.org/10.1016/j.egyr.2021.05.027.

[51] S. Ha, G. Pozzato, S. Onori, J. Solid State Electrochem. 28 (3–4) (2023) 1131–1157, http://dx.doi.org/10.1007/s10008-023-05717-1.

[52] P. Rodríguez-Iturriaga, D. Anseán, S. Rodríguez-Bolívar, V.M. García, M. González, J.A. López-Villanueva, Appl. Energy 353 (2024) 122141, http://dx.doi.org/10.1016/j.apenergy.2023.122141.

[53] P. Rodríguez-Iturriaga, V.M. García, S. Rodríguez-Bolívar, E.E. Valdés, D. Anseán, J.A. López-Villanueva, Appl. Energy 367 (2024) 123327, http://dx.doi.org/10.1016/j.apenergy.2024.123327.